Laser beam powder bed fusion of novel biomedical titanium/niobium/tantalum alloys: Powder synthesis, microstructure evolution and mechanical properties

Jan Johannsen [a], Christian Lauhoff [b], Melanie Stenzel [c], Christoph Schnitter [c], Thomas Niendorf [d], Markus Weinmann [c,*]

[a] Fraunhofer Einrichtung für Additive Produktionstechnologien, IAPT, Am Schleusengraben 14, 21029 Hamburg, Germany
[b] RMIT Centre for Additive Manufacturing, School of Engineering, RMIT University, Melbourne, VIC 3000, Australia
[c] Taniobis GmbH, Im Schleeke 78-91, 38642 Goslar, Germany
[d] Universität Kassel, Institut für Werkstofftechnik, Metallische Werkstoffe, Mönchebergstr. 3, 34125 Kassel, Germany

ARTICLE INFO

ABSTRACT

The synthesis of spherical titanium/niobium/tantalum (TNT) alloy powders, namely Ti-20Nb-6Ta, Ti-27Nb-6Ta, Ti-35Nb-6Ta, and Ti-22Nb-19Ta (in wt-%) by electrode induction melting gas atomization is reported. The powder materials are characterized in detail using X-ray diffraction and scanning electron microscopy. Their processability via laser beam powder bed fusion (PBF-LB/M) is proven, and microstructure as well as mechanical properties of the additively manufactured specimens are assessed. All powders feature a dendrite-type microstructure with Nb/Ta-rich dendritic and Ti-rich inter-dendritic phases. Crystal structures of the powders are strongly composition-dependent. Nb- and Ta-rich Ti-35Nb-6Ta and Ti-22Nb-19Ta feature a body-centered cubic lattice, whereas Ti-rich Ti-20Nb-6Ta and Ti-27Nb-6Ta powders are characterized by multi-phase microstructures, consisting of non-equilibrium martensitic phases. Processing by PBF-LB/M causes significant changes in their microstructures: the dendrite-type morphologies vanish, and the formation of microstructures with a homogeneous element distribution can be observed in all additively manufactured parts. Ultimate tensile strength (UTS) as well as elongation at fracture are assessed by tensile testing. UTS values are found to be in a range from 651 MPa (Ti-35Nb-6Ta) to 802 MPa (Ti-20Nb-6Ta); strain-to-failure is between 21.3 % (Ti-35Nb-6Ta) and 31.7 % (Ti-22Nb-19Ta). Ductile fracture behavior is seen for all TNT alloys investigated.

1. Introduction

Titanium and its alloys, such as Ti-6Al-4V and Ti-6Al-7Nb (if not explicitly indicated, then all values are given in wt-%), are state-of-the-art implant materials [1-7]. These materials feature good biocompatibility, i.e., cell tolerance and osseointegration. Ti-6Al-4V and Ti-6Al-7Nb are preferred over commercially pure titanium (CP-Ti) due to their higher strength and superior corrosion resistance [8,9]. The latter results in a reduced release and exposure of metal ions into the human organism. Accordingly, implant-associated inflammations are likewise reduced [10].

However, an detrimental issue of CP-Ti, Ti-6Al-4V and Ti-6Al-7Nb for implant integration in the human body is their high Young's moduli ranging from 108 to 115 GPa. Highly diverging elastic properties

of implant and cortical bone (Young's modulus of 12 – 25 GPa) promote stress-shielding effects at the implant-bone interphase [11,12]. Therefore, bone ingrowth, i.e., osseointegration of the implant, can be unfavorably affected and, thus, implant loosening and/or osteolysis may occur [13,14]. Moreover, the application of Ti-6Al-4V as an implant material must be questioned due to toxicological concerns: vanadium has been shown to be toxic [15,16] and aluminum is suspected to cause Alzheimer's disease [17-19]. Replacement of these elements in permanent implants is consequently anticipated.

In the last two decades, extensive work has been carried out to explore novel biocompatible Ti-based alloys, featuring mechanical properties being close to those of human bone [3,5,6,20,21]. Promising new alloy systems are characterized by a favorable combination of high elasticity (a low Young's modulus), high strength, good fatigue

properties and sufficient biocompatibility. Binary, ternary as well as higher-component systems and, recently, even Ti-based high-entropy alloys have been introduced for use as metallic implant materials [22,23,24]. To prove biocompatibility, many efforts have been made in recent studies to assess the interaction of human cells with these alloys. From the results obtained it was concluded that bio-tolerant refractory metals (RM) such as Zr, Hf, Nb and Ta seem to be very promising as alloying elements.

Among the binary systems, Ti/Nb [25,26,27,28,29] and Ti/Ta [30,31,32,33] seem to be the most promising materials for application in orthopedic implants. Alloying Ti with either Nb or Ta leads to similar characteristics since Nb and Ta are each β-phase stabilizing elements featuring highest biocompatibility [34,35,36]. Conventionally processed Ti-based alloys with low Nb or Ta content show a martensitic α′-phase microstructure at room temperature (RT). With increasing Nb or Ta contents, in turn, the formation of martensitic α″-, dual β + α″-, or single β-phase alloys are observed [30]. The Young's moduli are concentration-dependent in both systems, featuring two minima for each alloy, i.e., Ti-16Nb and Ti-42Nb as well as Ti-30Ta and Ti-70Ta, respectively [37]. The lowest moduli are observed for body-centered cubic (bcc) β-phase microstructures, i.e., for Nb- and Ta-rich alloys.

Combining Ti with both Nb and Ta, leads to ternary Ti/Nb/Ta alloys, which have also attracted scientific attention. Even though some alloy compositions have been proven to exhibit shape memory effect or superelasticity [38,39,40], the scientific focus is predominantly on biomedical applications. Bertrand et al. investigated Ti-25Nb-25Ta processed by cold crucible levitation melting [41,42]. Tensile tests for this β-phase alloy revealed a very low Young's modulus of about 55 GPa as well as good ductility and strength, i.e., 20 % elongation at fracture and about 530 MPa UTS. Biocompatibility, i.e., corrosion behavior and cytotoxicity of Ti-30Nb-18Ta (in the original publication referred to as $Ti_{77}Nb_{17}Ta_6$) and partially oxidized Ti-30Nb-18Ta(O) alloys were reported by Husein et al. and compared with Ti-6Al-4 V [43]. The arc-melted, solution-treated and finally 50 % cold-rolled material predominantly consisted of the orthorhombic α″ martensitic phase embedded in a β-phase matrix. A comparison of the corrosion current density of Ti-30Nb-18Ta, Ti-30Nb-18Ta(O) and Ti-6Al-4V clearly revealed an efficient passivation of Ti-30Nb-18Ta due to the presence of Nb and Ta, both forming chemically inert native oxide surfaces.

Powder metallurgical approaches for fabricating Nb-25Ti-xTa (x = 10, 15, 20, 25, 35 at-%) alloys have been reported by Liu et al., [44]. Green compacts were sintered at 1600, 1700 and 1800 °C in a vacuum (10^{-3} Pa) for 2 h, followed by investigations on their relative densities, mechanical strength and Young's moduli. Interestingly, due to Ta particle segregation dispersion strengthening of the materials was observed with increasing Ta content.

The focus of the present study is on TNT alloys in the Ti-rich domain for medical applications, i.e., dental and orthopedic implants with the highest level of biocompatibility. To keep the density of the targeted implants low, Nb ($\rho = 8.57$ g/cm^3) was used as the main alloying constituent, whereas Ta ($\rho = 16.65$ g/cm^3) was added in lower concentration. Accordingly, Ti-xNb-6Ta (x = 20, 27, 35 wt-%) alloys were fabricated and characterized in depth. For comparison, Ti-22Nb-19Ta containing almost equal contents of Nb and Ta, was also produced and investigated.

TNT powder materials have been prepared from pre-alloyed electrodes by electrode induction melting gas atomization (EIGA) [45,46]. The powders were chemically and structurally characterized in detail and conditioned for application in additive manufacturing (AM) technologies, i.e., for PBF-LB/M. In the biomedical sector, this technology offers great potential to produce personalized orthopedic implants with highest fitting accuracy [47,48]. The required patient-specific structural data for creating a 3D model can easily be obtained from examinations using computed tomography (CT) or magnetic resonance imaging (MRI) [49,50].

2. Materials and methods

2.1. Powder synthesis and refinement

Spherical titanium/niobium/tantalum (TNT) powders were obtained from pre-alloyed electrodes by EIGA conducted under purified argon (4.6, Linde) atmosphere [51]. The nominal chemistry as well as chemical compositions of the powder materials determined by inductively coupled plasma optical emission spectroscopy (ICP-OES; Analytik Jena PlasmaQuant PQ 9000/9100), carrier gas hot extraction (LECO TCH-600/ONH-836) and/or combustion analysis (LECO CS-744) are listed in Table 1.

As the as-atomized powders featured minor fractions of coarse and/or irregular-shaped particles, all powder materials were sieved using 150 μm meshes. In the following, the powders were transferred into an air classifier for deagglomeration and removal of fine particles < 10 μm to improve flow properties and avoid dusting during the manufacturing process. From the remaining powders, the PBF-LB/M particle size fraction (10 – 63 μm) was extracted by ultrasonic sieving with 63 μm meshes. Particle size distributions (PSD) were determined using a Master Sizer 2000 (Malvern, Worcestershire, United Kingdom).

2.2. Laser beam powder bed fusion

PBF-LB/M was performed using a commercially available system (3D Systems, DMP350 Flex) equipped with an 1 kW single-mode laser (YLR-1000-WC-Y14 by IPG). Argon gas was used as shielding gas to prevent oxidization during manufacturing. The oxygen concentration of the closed build chamber was kept below 50 ppm during processing. To evaluate suitable processing windows, cuboids of 10 × 10 × 11 mm^3 in size were fabricated. A stripe based, bi-directional scanning strategy with a stripe width of 5 mm (cf. Fig. 1) was employed, while the scanning direction was rotated by 67° from layer to layer. Heating of the base plate was not applied, even though such heating has been numerously reported to be advantageous for PBF-LB/M processing, especially when less ductile Ti alloys and intermetallics are processed [52]. However, as will be shown below, the TNT powder materials studied in the present work show excellent processability at RT.

In order to elaborate adequate process parameter windows, laser power (P_L) and scan speed (v_s) were varied between 135 and 280 W and 1050 – 1500 mm/s, respectively. The hatch distance (H_s) was kept constant at 69 μm, while the powder layer thickness was set to 30 μm. Resulting energy per unit area (E_A) values were calculated by: [53]

$$E_A \left(\frac{J}{mm^2} \right) = \frac{P_L(W)}{v_S\left(\frac{mm}{s}\right) \bullet H_S(mm)}$$

Following porosity analysis (details are given in Section 3.2), for each TNT alloy the set of process parameters leading to the highest density value was used to fabricate specimens for mechanical testing. Stacks of flat tensile test specimens (blocks of 12 mm in height, Fig. 2) were manufactured and cut into 2 mm thick slices using electrical discharge machining (EDM).

2.3. Microstructural and mechanical characterization

For residual porosity analysis, the initially PBF-LB/M processed

Table 1
Chemical compositions of the TNT powders after gas atomization.

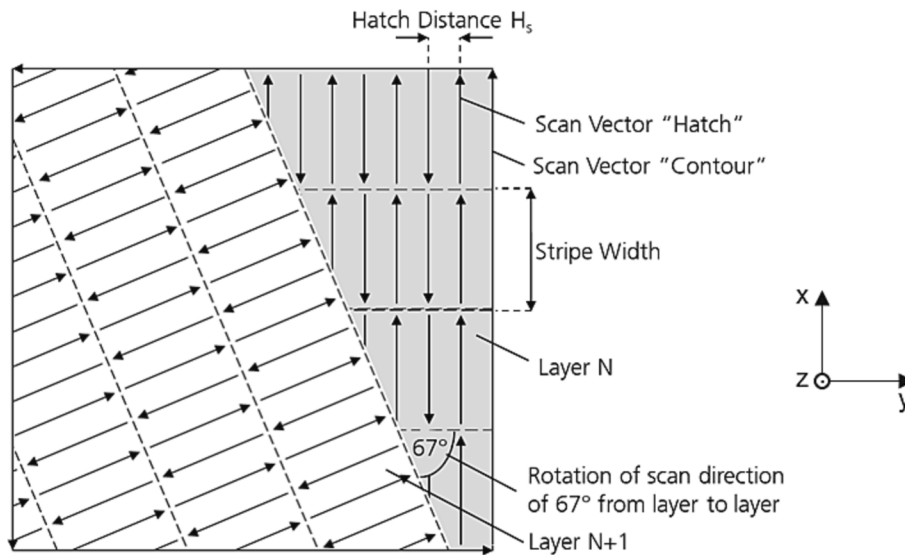| Nominal	wt-%			ppm			
	Ti	Nb	Ta	C	H	N	O
Ti-20Nb-6Ta	73.75	19.98	5.96	73	<45	74	2556
Ti-27Nb-6Ta	66.98	26.94	6.02	51	<10	206	2278
Ti-35Nb-6Ta	58.87	34.45	5.98	33	<10	147	1791
Ti-22Nb-19Ta	59.02	21.79	18.58	32	13	93	2409

Fig. 1. Schematic illustrating the scan strategy used for PBF-LB/M processing: a bi-directional stripe scanning strategy for the core and a one vector width contouring strategy. From layer to layer the scanning direction was rotated by 67° counterclockwise.
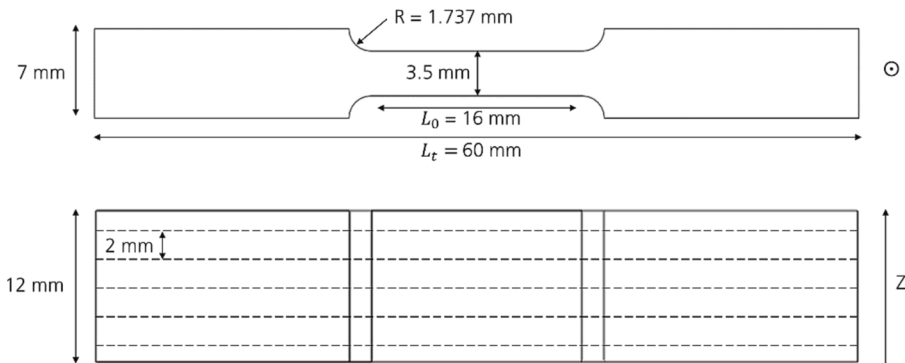

Fig. 2. Schematic showing the tensile specimen geometry with a gauge length (L_0) of 16 mm. A stack of flat tensile specimens was manufactured according to the final contour (in the X-Y plane) and cut into 2 mm thick slices.

cuboids were cut parallel and perpendicular to the build direction (BD) using EDM, followed by mechanical grinding and polishing. Optical micrographs of the surfaces recorded using light microscopy (LM, VHX-5000 by KEYENCE) were converted to black and white, enabling the calculation of the porosity from the number of black and white pixels. For initial microstructure analysis via LM, the specimens were additionally etched for 45 s using a solution of ammonium persulphate and sodium fluoride in deionized water (TitanEtch by Titan Tech Europe). Moreover, scanning electron microscopy (SEM) including energy dispersive X-ray spectroscopy (EDS) and electron backscatter diffraction (EBSD) were employed. EDS analysis was conducted on both polished powder particle cross-sections as well as additively manufactured specimens to assess the local and global (average) chemical composition of the TNT powders and the bulk materials after processing, respectively. For EBSD, specimens were mechanically ground and electropolished for 35 s at 30 V and 1.1 A using A3 electrolyte (Struers). Employing a Panalytical X-ray diffractometer (Almelo, Overijssel, Netherlands; X'Pert MPD-PRO, Cu Kα radiation), X-ray diffraction on the TNT powders and as-built specimens was conducted with Cu Kα radiation in a 2θ range between 10 and 80° to assess the phase composition. Indexing of the diffractograms was performed using the ICDD pdf-2 database [54].

To investigate the mechanical properties, quasi-static uniaxial tensile tests were conducted on a ZwickRoell AllroundLine 10kN testing machine at RT in displacement control with a nominal strain rate of 0.0067 s^{-1} [55]. Strains were calculated based on the crosshead displacement and the gauge length of the specimens.

3. Results and discussion

3.1. Powder synthesis and characterization

The PSDs of all TNT alloy powders following sifting and subsequent sieving (cf. **Section 2.1**) with 63 μm meshes are shown in Fig. 3. All powders feature a monomodal distribution. While for the Ti-22Nb-19Ta powder a small number of particles with diameters in the range of 5 – 12 μm is present, particles smaller than 15 μm are not found in the other powder materials. In case of Ti-22Nb-19Ta, however, the minor 5 – 12 μm fraction observed has no obvious detrimental effect on the flow properties of the powder material, as determined by Hall Flow testing according to ASTM B213-20 [56]. The upper particle size was limited by the 63 μm mesh width and, thus, D95 values are between 63 and 69 μm for the different powders.

Fig. 4 displays SEM results of the powder materials. The secondary electron (SE) images proof that all TNT alloys are obtained as highly spherical particles, featuring smooth surfaces without visible cracks. Ti-20Nb-6Ta (Fig. 4a) and Ti-27Nb-6Ta (Fig. 4b) particles are fully deagglomerated, whereas minor agglomeration is observed for the other two alloy powders. However, the marginal degree of agglomeration did not cause any issues during PBF-LB/M processing. Structures of highest
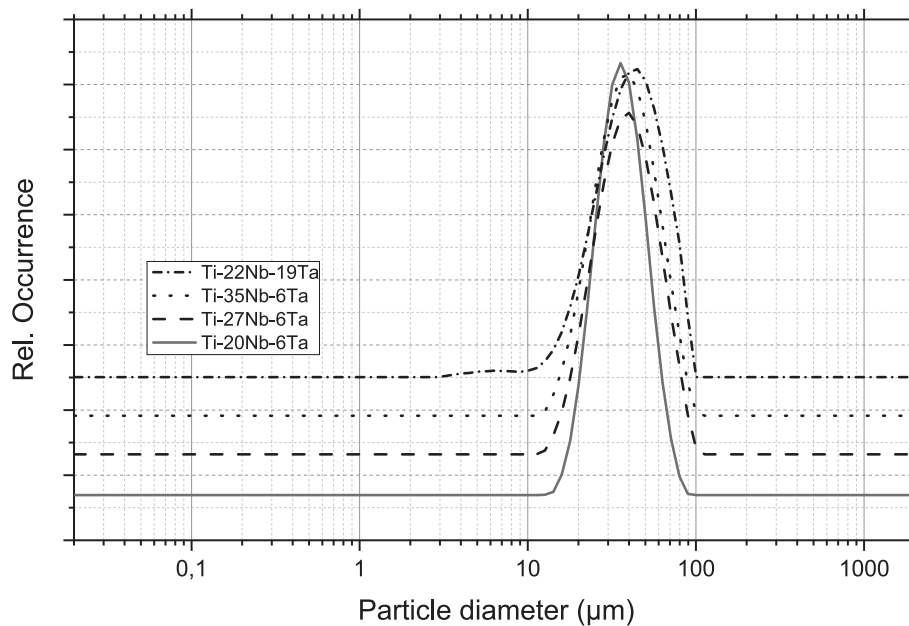
Fig. 3. Particle size distribution of the TNT alloys after sifting and sieving.
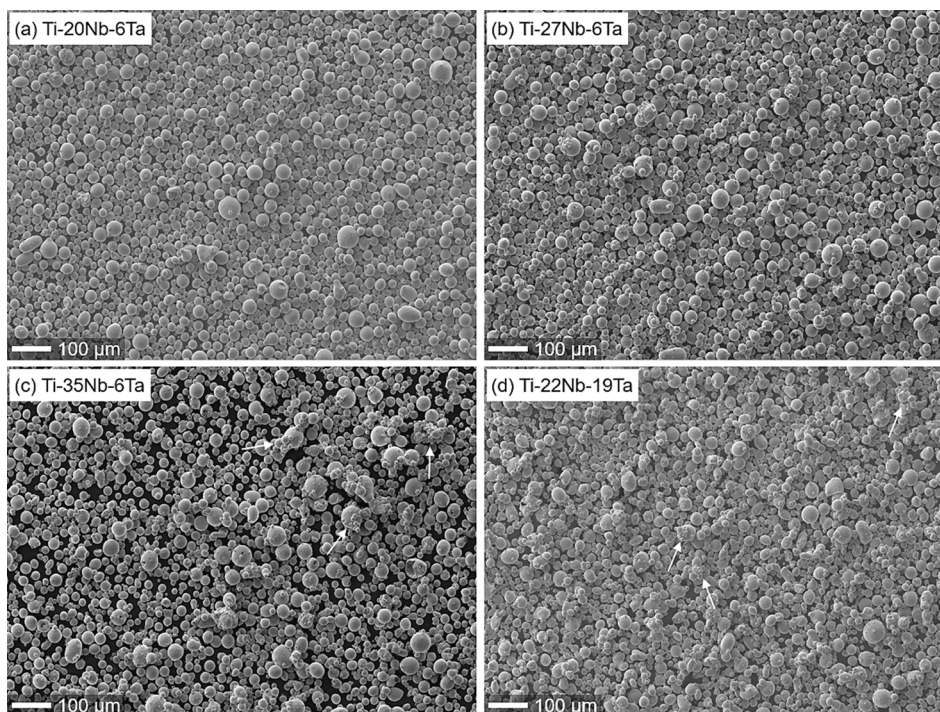

Fig. 4. SEM images of the TNT alloy powders after sifting and sieving. White arrows in (c) and (d) highlight agglomerations found in case of the Ti-35Nb-6Ta and Ti-22Nb-19Ta powders.

density could be obtained for each material as shown below (cf. Fig. 7 and Table 3).

SEM/EDS results of polished cross-sections are provided in Fig. 5, showing particles with a dense, pore-free morphology. Quantitative results of the local and the overall chemistry are listed in Table 2. The TNT powder particles exhibit a dendrite-type microstructure with noticeable chemical fluctuations between dendritic and inter-dendritic regions. The overall chemical composition of the particles (areas 5 in Fig. 5 and Table 2) is in good agreement with data experimentally determined by ICP-OES (cf. Table 1). Only the Ti values are determined

slightly too high in the EDS analysis. Accordingly, Nb and Ta values are generally found to be slightly too low, except for Ti-35Nb-6Ta, in which an overall content of 6.5 wt-% of Ta is determined by EDS. For example, EDS of Ti-20Nb-6Ta (entire particle, area 5) reveals an overall composition of Ti-17.4Nb-5.3Ta. The deviations from the data experimentally determined by ICP-OES are: Ti + 3.3 wt-%, Nb −2.6 wt-%, Ta −0.7 wt-%.

Assessment of the local chemistry within the individual specimens (cf. spots 1 − 4 in Fig. 5 and Table 2) reveals different chemical compositions for the dendritic and inter-dendritic regions. For example,
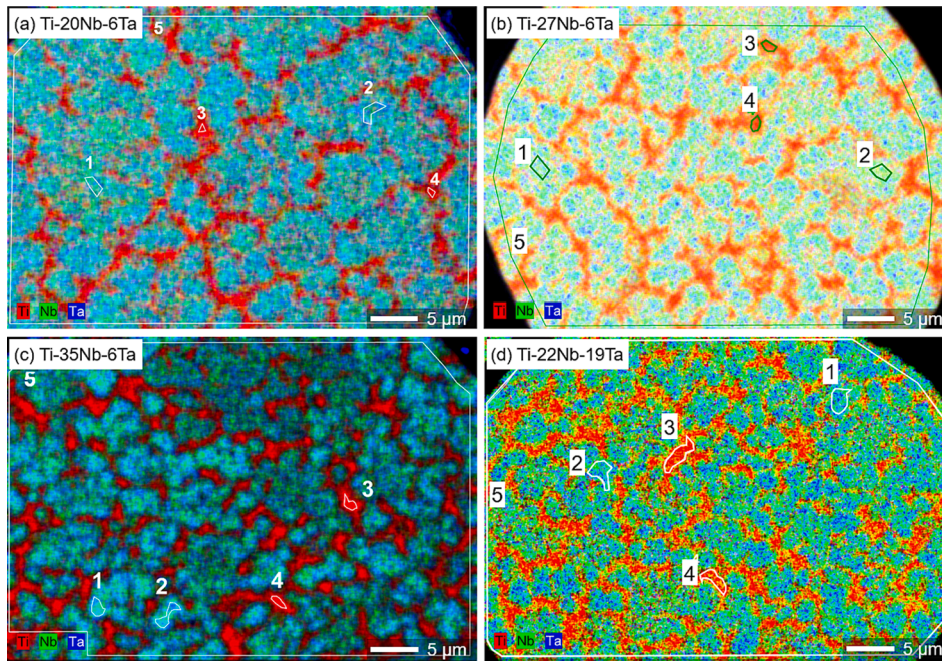
Fig. 5. SEM/EDS cross-section mappings of the TNT alloy powder particles. The chemical composition was determined locally in dendritic (spots 1, 2) and inter-dendritic regions (spots 3, 4), as well as globally (area 5). Quantitative results are provided in Table 2.

Table 2
Quantitative EDS results revealing the chemical compositions (in wt-%) of the TNT alloy powders. Spots 1 – 4 and area 5 investigated are marked in Fig. 5. ICP-OES data are listed for comparison.

Nominal		1	2	3	4	5	ICP-OES
Ti-20Nb-6Ta	Ti	74.5	77.0	85.0	81.4	77.3	74.0
	Nb	19.6	17.9	13.2	16.0	17.4	20.0
	Ta	5.9	5.1	1.9	2.7	5.3	6.0
Ti-27Nb-6Ta	Ti	65.1	66.8	77.0	74.8	68.9	66.5
	Nb	29.2	27.5	21.0	21.9	25.5	26.8
	Ta	5.8	5.6	2.1	3.3	5.6	6.1
Ti-35Nb-6Ta	Ti	60.9	61.9	73.2	71.6	62.0	59.0
	Nb	32.0	31.9	24.6	25.0	31.6	35.0
	Ta	7.0	6.5	2.2	1.1	6.4	6.0
Ti-22Nb-19Ta	Ti	57.2	57.3	70.6	69.6	61.9	59.0
	Nb	20.5	20.3	16.9	17.1	19.2	22.0
	Ta	22.3	22.4	12.5	13.3	18.8	19.0

Table 3
Process parameters and resulting energy per unit area (E_A) found to lead to the highest density in the TNT alloys investigated.

| TNT alloy	Laser energy	Scan speed	E_A value	Relative density
Ti-20Nb-6Ta	170 W	1250 mm/s	1.97 J/mm^2	99.96 ± 0.01 %
Ti-27Nb-6Ta	170 W	1350 mm/s	1.83 J/mm^2	99.97 ± 0.01 %
Ti-35Nb-6Ta	170 W	1500 mm/s	1.64 J/mm^2	99.97 ± 0.01 %
Ti-22Nb-19Ta	230 W	1500 mm/s	2.22 J/mm^2	99.97 ± 0.03 %

while spots 1 and 2 in Ti-20Nb-6Ta (Fig. 5a) reveal a composition of Ti-19.6Nb-5.9Ta and Ti-17.9Nb-5.1Ta for the dendritic phase, the compositions of spots 3 and 4, both located in the inter-dendritic area, are Ti-13.2Nb-1.9Ta and Ti-16.0Nb-2.7Ta, respectively. Similar results are observed for the other TNT alloys. Table 2 points out that the differences in the contents of Ti, Nb and Ta are up to about 10 wt-%, 6 wt-% and 4 wt-%, respectively.

The occurrence of dendrite-type solidification microstructures is thought to be related to the characteristic cooling rates during powder synthesis. In contrast to PBF-LB/M processes, the inherent cooling rates during EIGA are not sufficiently high to fully prevent segregation

processes. During solidification which takes place at the solid/liquid interface, preferential crystallization of niobium (2477 °C) and tantalum (3017 °C) occurs due to their significantly higher melting points compared to titanium (1668 °C). As a result, niobium and tantalum are enriched in the dendritic structures which initially form, while titanium accumulates in the inter-dendritic domains. Such observations have also been reported for other high-alloyed materials with significant differences in the melting points of the constituents, e.g., gas-atomized Ti-42Nb [57], Al-modified Ti-Ta alloy [58] or low-density Al-steels [59]. Against this, the microstructures of the additively manufactured TNT specimens, which are discussed below, do not comprise dendritic features. Due to the very high cooling rates of 1 – 40 K/µs in the PBF-LB/M process, a homogeneous distribution of all constituting elements is finally obtained [60].

One of the main motivations for varying the chemistry in the present study is to assess the influence of the chemical composition on the phase evolution and mechanical properties of bulk structures fabricated from the powder feedstock. It is well known that Ti-based alloys can exist in different phases and solidification microstructures as well as phase compositions [61,62]. Ti-rich alloys typically reveal a hexagonal close-packed (hcp) structure, also known as the α-phase, or mixtures of hcp and bcc (β-phase) phases, also referred to as α + β. Heating of α-phase alloys leads to a reversible phase transformation into the high-temperature bcc β-modification, which transforms back into the original hcp α-phase upon cooling [63]. The addition of so-called β-stabilizing elements lowers the transformation temperature. Alloys with high contents of β-stabilizers can retain in the β-phase modification even down to RT and below. The α- and β-phase can be converted into one another by diffusionless transformations [64,65]. The orthorhombic ω-phase and the non-equilibrium martensitic α'- (hexagonal) and α''-phase (orthorhombic) are to be named in this regard [66,67,68].

Fig. 6a depicts the XRD diffractograms of the TNT powder materials after sifting and sieving, clearly revealing the influence of the chemistry on the phase evolution. In line with pure Nb, whose XRD pattern is plotted as a reference, the alloys with high content of Nb and Ta, i.e., Ti-22Nb-19Ta and Ti-35Nb-6Ta, only reveal reflections attributed to the bcc β-phase. A reduction of the Nb/Ta content leads to significant changes in the phase constitution. Accordingly, the diffractograms
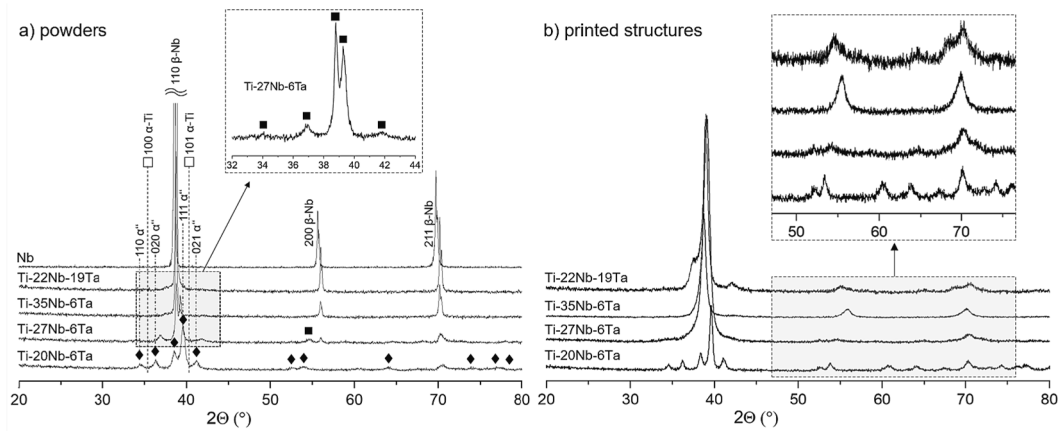
Fig. 6. XRD patterns of the TNT alloy powders after sifting and sieving (a) and after PBF-LB/M (b). For comparison, a characteristic pattern of pure Nb powder is plotted in (a). Rhombs in the diffractograms of Ti-20Nb-6Ta powders indicate reflections related to the orthorhombic α″ martensite, while diffraction peaks marked with squares (Ti-27Nb-6Ta) cannot be assigned unequivocally. Black-framed squares indicate the theoretical peak positions of the hcp α-phase being absent in any of the materials.
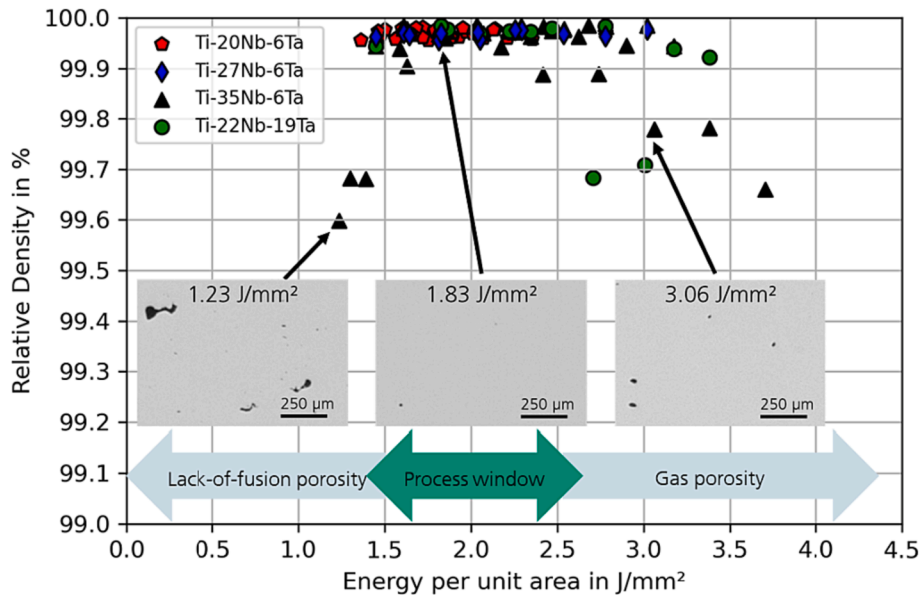
Fig. 7. Optically determined relative densities of the PBF-LB/M processed TNT alloys in relation to the energy per unit area (E$_A$). The insets depict optical micrographs of Ti-35Nb-6Ta processed with different E$_A$ values that are characterized by lack-of-fusion porosity, gas porosity and keyholing, respectively.

obtained for Ti-27Nb-6Ta and Ti-20Nb-6Ta indicate the formation of structures with reduced symmetry. For Ti-20Nb-6Ta, the reflections can be assigned to the orthorhombic α″-phase, indicating a fully martensitic microstructure. In case of Ti-27Nb-6Ta, however, a reliable assignment of the indentified reflections is challenging. The section highlighted in Fig. 6a (2θ range from 32 to 44°) displays two high-intensity peaks at 38.8 and 39.3°. In addition, low-intensity peaks are observed at 34.0, 37.0 and 41.7°. The peak positions of the dominant reflection at 38.8° as well as of those at higher angles (56.0 and 70.4°) indicate that the Ti-27Nb-6Ta powder features a bcc β-phase component in addition to another phase that cannot be assigned unequivocally. The theoretical peak positions of the hcp α-phase are also provided in Fig. 6 (dashed lines, open squares; intensities exceeding the background level are not seen at these positions). A more detailed phase analysis will be subject of future work.

Remarkably, processing by PBF-LB/M (cf. section 3.2) has only a minor influence on the appearance of the XRD patterns and, thus, on the phase constitution. The patterns of the AM processed samples appear to be very similar to those of the powders, especially with respect to the

location of the reflections. An obvious difference, however, is the appearance of reflections in the XRD patterns of the as-built materials, particularly the 200 and 211 β reflections, which are clearly broadened. This is most likely an effect of the prevailing microstructure and the crystallite sizes, respectively, which are smaller due to the rapid cooling in PBF-LB/M. This aspect is discussed in section 3.5 in more detail.

3.2. Laser beam powder bed fusion (PBF-LB/M)

Following processing, the process parameter windows were assessed by optical density measurements conducted on the PBF-LB/M manufactured cuboids. Depending on the energy per unit area (E$_A$), significant differences in the degree of residual porosity are found. In the inset of Fig. 7, three representative micrographs of Ti-35Nb-6Ta are displayed, showing aspherical lack-of-fusion porosity (E$_A$ = 1.23 J/mm^2), minor residual porosity (E$_A$ = 1.83 J/mm^2), and keyholing (E$_A$ = 3.06 J/mm^2). Finally, for all TNT alloys investigated, high density parts with relative densities > 99.9 % were obtained in the process window of 1.5 J/mm^2 < E$_A$ < 2.5 J/mm^2. Table 3 summarizes the sets of process parameters and

the resulting E_A values, leading to the highest density value in each TNT alloy. These parameters were used to manufacture the flat tensile specimens for mechanical characterization (cf. **Chapter 2** and section 3.4).

3.3. Microstructure of PBF-LB/M processed parts

As detailed above, the TNT powder particles feature localized chemical fluctuations, i.e., dendritic micro-segregations after EIGA processing (Fig. 5). Using the PBF-LB/M technique, metallic materials are melted by a laser beam and rapid solidification occurs due to the small melt pool dimensions in combination with the high thermal conductivity of the alloys fabricated. As mentioned above, cooling rates of 1 – 40 K/μs and thermal gradients in the range of 5 – 20 K/μm have been reported [60], eventually promoting the formation of metastable phases in PBF-LB/M processed structures. These differ significantly from those observed in the initial powder feedstocks or structural features determined in conventionally cast components [69].

The morphological and microstructural properties of the PBF-LB/M processed TNT alloys were examined by LM and SEM including EDS and EBSD. The optical micrographs shown in Fig. 8 give clear evidence that the chemistry has a significant impact on the structure/phase

formation. Differences can be seen in the microstructure between the Ti-richest alloy (Ti-20Nb-6Ta, Fig. 8a) and the three others. The micrograph of Ti-20Nb-6Ta recorded at higher magnification (Fig. 8e) illustrates three main characteristic features: (1) elongated, columnar grains oriented along BD (grain boundaries are highlighted by white dotted lines), (2) platelet-like structures featuring an angle of 45° with respect to BD (marked by white arrows), and (3) the melt pool boundaries (marked by white triangles). The depth of the melt tracks is about 160 μm. The width of the columnar grains is up to 120 μm, whereas their long axis can be in the millimeter range. Obviously, these grains comprise both the platelet-like structures and the melt pool boundaries. It must be noted at this point that the platelet-like structures are not visible in the micrographs of Ti-27Nb-6Ta, Ti-35Nb-6Ta, and Ti-22Nb-19Ta. Furthermore, the tendency to form a highly anisotropic microstructure, i.e., extensive formation of columnar grains, seems to decrease with decreasing Ti content, as can be deduced from Fig. 8a-d.

Fig. 9 presents SEM/EDS results for the TNT alloys after PBF-LB/M processing. It has to be noted that the platelet-like structures observed in Ti-20Nb-6Ta (Fig. 9a) via LM cannot be resolved in the corresponding EDS mapping. However, the EDS results give a clear indication for minor segregations along the melt pool boundaries into Ti- and Nb/Ta-rich domains. The local chemical compositions of specific spots, such as
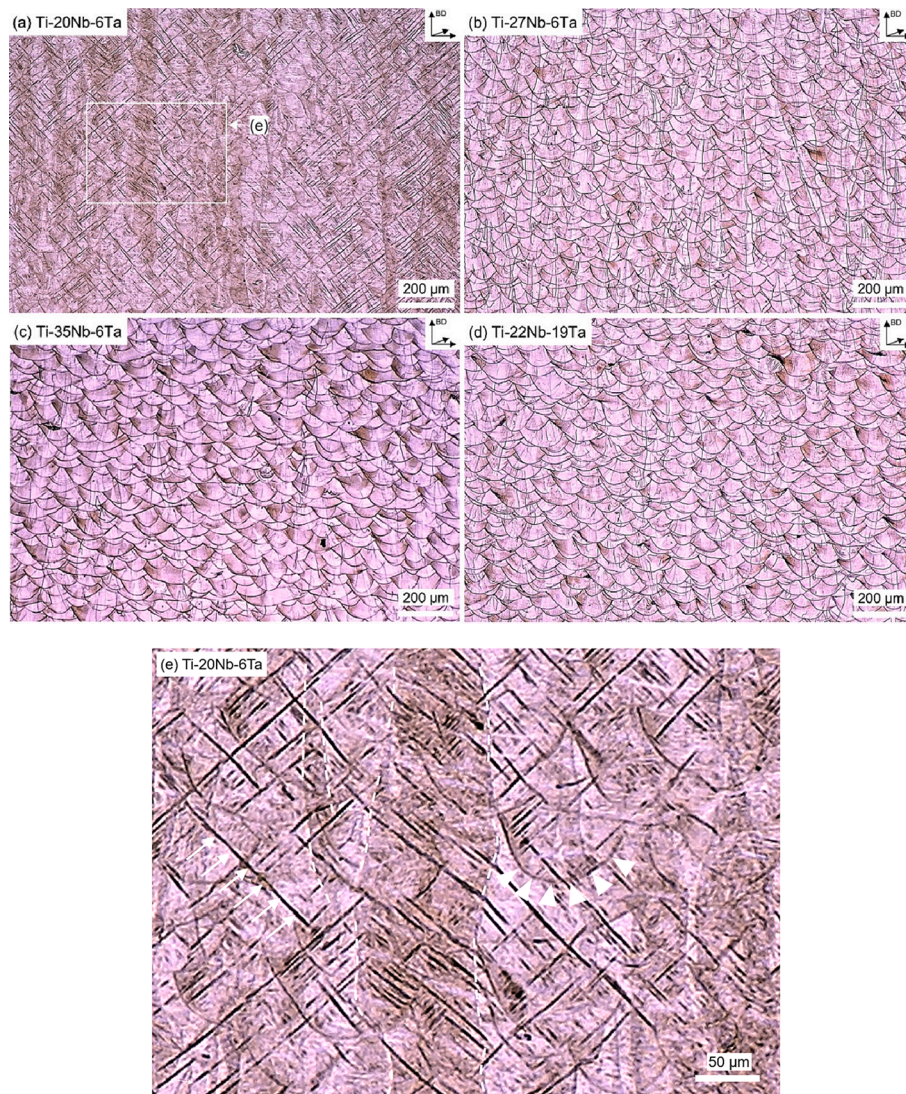
Fig. 8. Optical micrographs of the PBF-LB/M processed TNT alloys in the as-built condition: Ti-20Nb-6Ta (a), Ti-27Nb-6Ta (b), Ti-35Nb-6Ta (c), and Ti-22Nb-19Ta (d). Platelet-like structures, elongated (columnar) grains and melt pool boundaries are highlighted in the high-magnification image in (e), by white arrows, dotted lines, and white triangles, respectively.
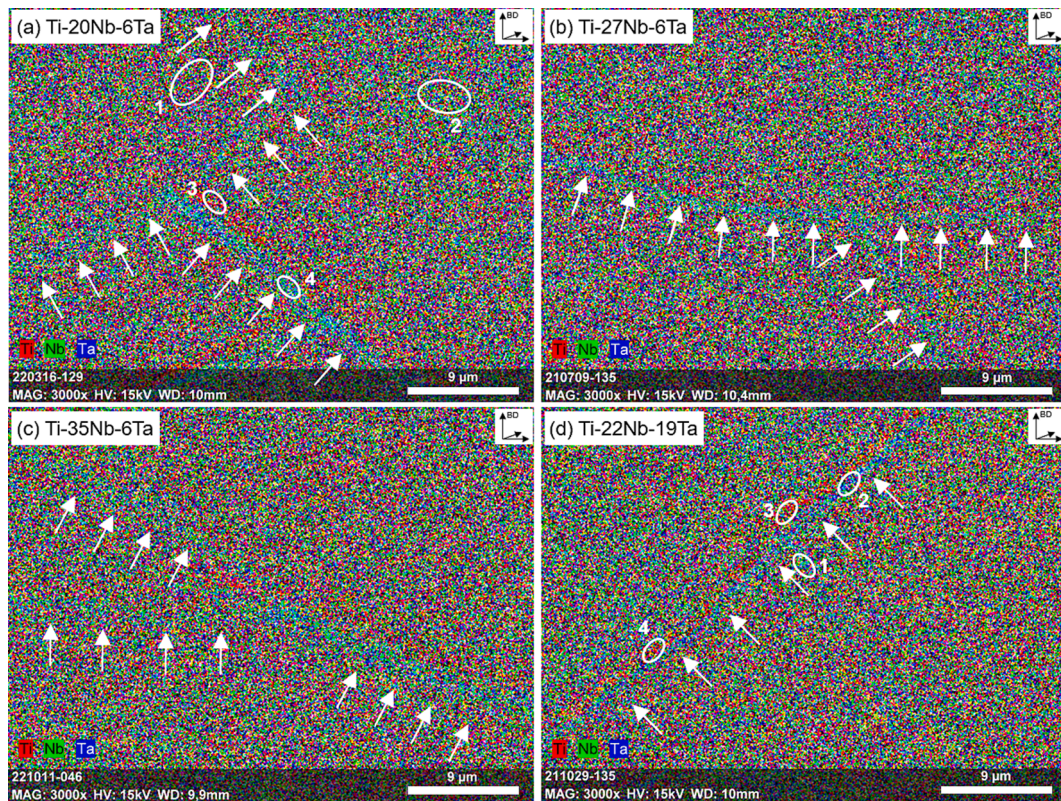
Fig. 9. EDS mappings of the PBF-LB/M processed TNT alloys in the as-built condition: Ti-20Nb-6Ta (a), Ti-27Nb-6Ta (b), Ti-35Nb-6Ta (c), and Ti-22Nb-19Ta (d). Arrows highlight minor chemical segregations along the melt pool boundaries. Chemical compositions of selected spots of Ti-20Nb-6Ta and Ti-22Nb-19Ta are provided in Table 4.

grain boundaries, as well as the overall composition of two specimens, namely Ti-20Nb-6Ta and Ti-22Nb-19Ta, are exemplarily given in Table 4. Although the chemical variations are small, it is obvious that Nb and Ta are enriched at the outer (colder) part of the melt tracks, while Ti is preferentially found in the inner regions (in BD). For example, in case of Ti-20Nb-6Ta the average Ti content (Fig. 9a, spot 1) is about 76.1 %. In contrast, the corresponding Ti values close to the melt pool boundary are 79.0 % in the inner part (Fig. 9a, spot 3) and 74.7 % in the outer part (Fig. 9a, spot 4). Despite these minor chemical fluctuations, it must be emphasized that the EDS results display a very homogeneous element distribution for the additively manufactured TNT materials. This is in clear contrast to the dendrite-type microstructures observed on the same scale in the initial feedstock powder material (Fig. 5). Here it is important to note, that investigations of powder and additively manufactured bulk were performed using the same SEM equipment and almost similar experimental conditions.

To assess the crystallographic characteristics of each condition, the PBF-LB/M processed TNT alloys were analyzed using EBSD. Fig. 10 shows inverse pole figure (IPF) mappings recorded in the X-Y plane (i.e.,

perpendicular to BD).

Before EBSD analysis, the Ti-rich samples, i.e., Ti-20Nb-6Ta and Ti-27Nb-6Ta, were heat treated at 850 °C for 21 h under argon atmosphere to dissolve potential non-equilibrium martensitic phases. Eventually, this procedure allowed to investigate the (prior)-β-grain structure. EBSD data were additionally post-processed using OIM Analysis software (EDAX) and the grain dilation routine. In the IPF mappings, the β-phase was indexed using a cubic crystal structure (Im3m) and a lattice parameter of a = 0.3285 nm. As can be deduced from the EBSD results, all TNT alloys are characterized by a similar solidification behavior during PBF-LB/M processing:

(1) Due to the bi-directional scanning strategy, a checkerboard-like grain arrangement is formed within the X-Y plane, indicating a pronounced impact of epitaxy. Epitaxial solidification with elongated, columnar grains is also seen in the optical micrographs recorded parallel to BD (Fig. 8).

(2) The columnar grains feature a preferred crystallographic orientation, i.e., grains mostly oriented in ⟨001⟩ direction with respect to BD as well as in ⟨101⟩ and ⟨111⟩ direction with respect to the loading direction (LD) of the tensile specimens and the transversal direction (TD).

In a process parameter window being favorable for epitaxy, metallic materials, which solidify in a cubic phase, are known to solidify preferentially with the ⟨001⟩ direction alongside the direction of the maximum thermal gradient [70,71,72]. Due the maximum thermal gradient being mostly aligned in BD, the evolution of strongly ⟨001⟩ textured, columnar-grained microstructures alongside BD was reported for various cubic materials processed by different AM techniques [73,74,75]. In the present work, differences in terms of the intensity of texture are obvious among the TNT alloys investigated. These differences can be caused by differences in the process parameters employed (E_A values) and the chemistry. In case of higher contents of Nb and Ta, constitutional supercooling is thought to hamper epitaxial growth and

Table 4

Chemical compositions (in wt-%) of PBF-LB/M processed Ti-20Nb-6Ta and Ti-22Nb-19Ta determined from EDS measurements shown in Fig. 9. The spots used for assessment are marked with 1 – 4 in Fig. 9. The symbol $\sum$ corresponds to the EDS analysis of the entire region depicted.

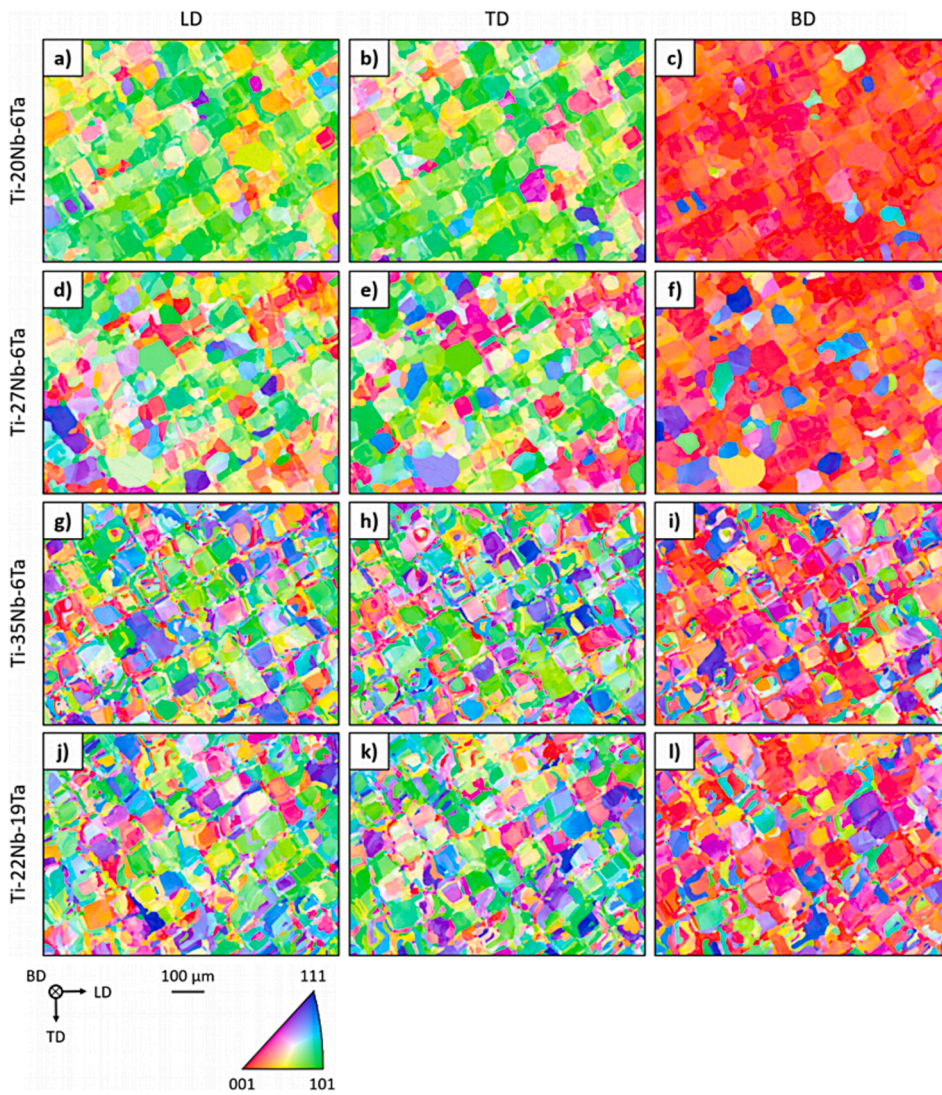| Spot	Ti-20Nb-6Ta			Ti-22Nb-19Ta		
	Ti	Nb	Ta	Ti	Nb	Ta
1	75.7	18.1	6.2	57.2	22.4	20.4
2	76.9	18.2	5.0	57.1	22.6	20.3
3	79.0	16.2	4.8	63.8	19.6	16.6
4	74.7	19.2	6.2	66.9	21.1	12.0
$\sum$	76.1	17.9	6.1	61.3	21.5	17.3

Fig. 10. SEM/EBSD inverse pole figure (IPF) mappings of the PBF-LB/M processed TNT alloys. The mappings recorded perpendicular to the building direction (BD) are plotted with respect to the loading direction (LD) of the tensile specimens (cf. Fig. 2) used for mechanical characterization (a,d,g,j), the transversal direction (TD) (b, e,h,k) and BD (c,f,i,l). The Ti-rich alloys, i.e., Ti-20Nb-6Ta and Ti-27Nb-6Ta, were heat treated before characterization to stabilize the bcc β-grain (solidification) structure for direct comparison of the four conditions. The reference coordinate system and the color-coded standard triangle are shown in the lower left.

promotes grain refinement [76]. A follow-up study is already in progress, detailing the influence of the scanning strategy and the process parameters on microstructural features and mechanical properties of PBF-LB/M processed Ti-27Nb-6Ta.

3.4. Mechanical properties

Fig. 11 shows representative tensile stress–strain curves for the PBF-LB/M processed TNT alloys in the as-built condition, i.e., without conducting a post-process heat treatment. The stress–strain curves of Ti-20Nb-6Ta, Ti-27Nb-6Ta and Ti-35Nb-6Ta are characterized by similar characteristics: the elastic regime is followed by a stress plateau, exhibiting plastic deformation at constant stress, and finally a ductile fracture behavior. The most important characteristic values obtained under monotonic tensile loading, i.e., UTS and elongation at failure, are given in Table 5.

UTS values for Ti-20Nb-6Ta, Ti-27Nb-6Ta, and Ti-35Nb-6Ta are 802 MPa, 739 MPa, and 651 MPa, respectively. In line with these values, it can be concluded that a decreasing Ti content (or accordingly an increasing Nb content) reduces the strengths of the TNT materials. This tendency, in turn, results from the different composition-dependent microstructures of the alloys. XRD investigations depicted in Fig. 6 clearly show that Nb/Ta-rich alloys only contain the bcc β-phase, whereas the Ti-rich alloys Ti-20Nb-6Ta and Ti-27Nb-6Ta feature

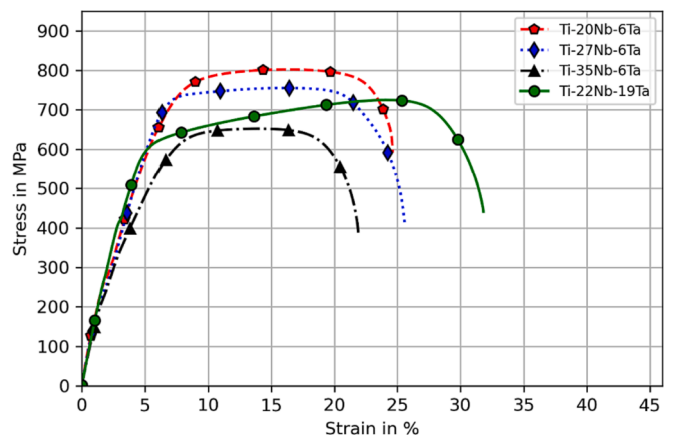**Fig. 11.** Representative tensile stress–strain curves of the PBF-LB/M processed TNT alloys in the as-built condition.

structures with reduced symmetry, e.g., the orthorhombic α″-phase. For Ti-20Nb-6Ta, a fully martensitic microstructure, and for Ti-27Nb-6Ta a multi-phase material state consisting of at least the α″- and β-phase are seen. Furthermore, the formation of reinforcing platelet-type structures

Table 5
Characteristic values obtained under monotonic loading extracted from the tensile tests shown in Fig. 11.

TNT alloy	Ultimate tensile strength (UTS)	Elongation at failure
Ti-20Nb-6 Ta	(802 ± 3.0) MPa	(24.2 ± 1.0) %
Ti-27Nb-6Ta	(739 ± 3.0) MPa	(26.0 ± 1.3) %
Ti-35Nb-6Ta	(651 ± 1.2) MPa	(21.3 ± 1.2) %
Ti-22Nb-19Ta	(717 ± 7.2) MPa	(31.7 ± 2.2) %

in Ti-20Nb-6Ta observed by LM (Fig. 8e) potentially contributes to increasing strength. Despite the differences in strength, the elongation at failure is quite similar for these alloys. Even though likewise characterized by a ductile fracture, Ti-22Nb-19Ta features a different stress–strain behavior. Following the onset of plastic deformation, the stress–strain curve reveals pronounced strain hardening. Failure occurs at about 31.7 % strain.

3.5. Process-microstructure-property relationships

The results presented and discussed in the sections before are the basis for an in-depth assessment of the TNT alloys studied in present work. In direct comparison to the powders processed by EIGA, the microstructures established by PBF-LB/M are distinctly different for all four alloys investigated here. This can be rationalized, as already highlighted before, by an extremely rapid cooling and solidification, both being characteristic for the PBF-LB/M process. Thus, non-equilibrium microstructures form, which may be rearranged and/or modified by a subsequent heat treatment. However, as the processing conditions in the additive manufacturing of all TNT alloys were very similar, differences observed in terms of microstructure evolution and mechanical properties can be attributed to the differences in chemical composition of the TNT alloys. The small differences in the laser energy input E_A applied during PBF-LB/M of the powders, probably only had a negligible influence on the results obtained.

If the alloying contents of Nb and Ta are relatively high, a β-phase microstructure is established upon PBF-LB/M. The solidification structure is characterized by relatively fine grains as evidenced by LM, EBSD, and XRD (Fig. 6b). Due to the high alloying contents, epitaxial growth of columnar β-phase grains is hampered. Instead, constitutional supercooling promotes fragmentation of the microstructure. As is highlighted by EBSD results and the checkerboard pattern seen, respectively, microstructure evolution seems to be close to the equiaxed-columnar transition. Thus, it is expected that major variations in the overall processing strategy will lead to pronounced differences in terms of microstructure evolution. Current work on this specific topic is underway and will be subject of follow-up studies.

For the two compositions with the highest Ti contents, significantly different phase compositions are observed. This is most obvious for the Ti-20Nb-6Ta alloy, whereas the Ti-27Nb-6Ta alloy seems to mark a transition region. In case of the latter, LM seems to reveal a β-phase microstructure, however, XRD analysis led to the conclusion that a second phase is present. As this second phase cannot be indexed reliably and is not visible in the micrographs, it is assumed that a nano-scaled phase formed, this phase being highly distorted. It is well-known that such phases cannot be reliably probed by lab-scale XRD, and that synchrotron-based assessment and/or transition electron microscopy (TEM) are needed to further characterize this condition.

The Ti-20Nb-6Ta alloy again can be fully assessed based on the results presented. EBSD analysis as well as LM suggest an epitaxial solidification, large columnar β-phase grains are visible. Texture intensities are highest and a preferred orientation of ⟨001⟩||BD, being characteristic for many alloys processed by AM, is seen. It should be emphasized that EBSD data for this condition stem from heat treated material, where the β-phase had been stabilized to allow for assessment of the solidification structure. In the as-built condition, a very specific pattern can be

seen in the micrographs obtained by LM. Plate-like structures are found in the entire volume probed. Even if not directly proven by the micrographs shown, these structures are attributed to a preferred selection of martensite variants. XRD analysis only revealed the presence of orthorhombic α″-phase, i.e., martensite. This is absolutely in line with many other Ti-base alloys, where the non-equilibrium martensite dominates the as-built microstructure. Its presence is rationalized by rapid cooling during PBF-LB/M. The preferred alignment of the plate-like structures in case of the Ti-20Nb-6Ta alloy can be rationalized based on the strong texture of the parent β-phase. EBSD revealed a preferred orientation not only for BD, but also for the other two directions assessed. Consequently, all columnar grains are oriented very similar. Due to the characteristic orientation relationships between the parent phase and the related martensite, traces of martensitic features must be very similar in every grain. Indeed, minor variations of the angle of traces can be seen in Fig. 8e when a grain boundary is crossed.

Looking at the monotonic properties characterized by tensile tests, the performance is good in all cases, i.e., high UTS values and high elongation at fracture are seen. The stress–strain response is obviously affected by the alloying concept, i.e., the only condition featuring a high Ta content (Ti-22Nb-19Ta) is characterized by significant hardening during the test. As the focus of the present work was on the conditions mainly alloyed by Nb, these conditions will be assessed in more depth. Looking at the results obtained for Ti-20Nb-6Ta, Ti-27Nb-6Ta and Ti-35Nb-6Ta, a decrease of UTS with increasing Nb content is obvious. The general characteristics of the stress–strain response indeed are very similar, dominated by the plateau-like behavior upon reaching the yield point. Derived from microstructure analysis employing LM and XRD, the main difference in these three alloys is the fraction of martensitic phases. Ti-35Nb-6Ta only shows peaks of the β-phase, Ti-20Nb-6Ta is fully martensitic, and Ti-27Nb-6Ta is a condition being mainly composed of bcc β-phase, however, containing most probably a nano-scale second phase (this phase not being indexed successfully so far). As the UTS of the respective alloys directly follows the trend derived from phase analysis, it is thought that martensite provides the most effective contribution to strengthening.

4. Conclusion

The microstructure and mechanical properties of novel Ti/Nb/Ta (TNT) powders and specimens processed by laser powder bed fusion, PBF-LB/M have been investigated. From the findings presented the following conclusions can be drawn:

1. TNT powders with spherical morphology are obtained by electrode induction melting gas atomization (EIGA). The phase composition of the as-atomized powders depends strongly on their chemical composition. In full agreement with conventionally processed Ti-based alloys, the fraction of β-stabilizers is of utmost importance for the prevailing microstructure. While an orthorhombic structure (α″) is observed in Ti-20Nb-6Ta, Ti-27Nb-6Ta features a multi-phase microstructure, at least consisting of a martensitic phase and the bcc β-phase. For an in-depth phase identification, future work is crucially needed. In turn, a further reduction of the Ti content, i.e., an increase in the Nb/Ta content, results in the formation of β-phase microstructures in Ti-35Nb-6Ta and Ti-22Nb-19Ta.
2. The spherical morphology of the TNT alloy particles makes them promising candidates for application in additive manufacturing processes. A wide process window for PBF-LB/M is revealed in the present study, yielding parts with > 99.96% relative density. While the powder materials feature a dendrite-type microstructure with slight local chemical fluctuations, the additively manufactured parts are characterized by a homogeneous element distribution.
3. Microstructure characterization after PBF-LB/M processing indicates significant differences in the microstructural evolution of the alloys. While all materials exhibit characteristic melt pool features, i.e., melt

tracks with depths of around 160 μm and elongated columnar grains oriented along the build direction (BD), platelet-like structures are observed solely in Ti-20Nb-6Ta.

4. The chemistry of the TNT alloys does not only influence the microstructural features, but likewise the mechanical properties. Ultimate tensile strength (UTS) clearly increases with increasing Ti content, which can be attributed to increasing volume fractions of the orthorhombic α''-phase, i.e., martensite. In contrast, the Nb/Ta-rich Ti-35Nb-6Ta and Ti-22Nb-19Ta alloys featuring single bcc β-phase microstructures do not contain reinforcing structural features and, thus, exhibit the lowest strengths of the TNT materials investigated.

5. The TNT materials examined were specifically developed for AM in the biomedical sector, e.g., for orthopedic and dental implants. Ongoing research is currently in progress, including mechanical testing under cyclic loading as well as biomedical investigations to elaborate the material interactions with human cells, i.e., osseointegration, vascularization and possible inflammatory reactions.

Declaration of Competing Interest

The authors declare that they have no known competing financial interests or personal relationships that could have appeared to influence the work reported in this paper.

Data availability

Data will be made available on request.

Acknowledgments

References

[1] M. Niinomi, C.J. Boehlert in Titanium Alloys for Biomedical Applications, Springer, Berlin, Heidelberg, 2000. https://doi.org/10.1007/978-3-662-46836-4_8.

[2] H.J. Rack, J.I. Qazi, Titanium alloys for biomedical applications, Mat. Sci. Eng. C 26 (2006) 1269–1277, https://doi.org/10.1016/j.msec.2005.08.032.

[3] A.T. Sidambe, Biocompatibility of advanced manufactured titanium implants – a review, Materials 7 (2014) 8168–8188, https://doi.org/10.3390/ma7128168.

[4] M. Long, H.J. Rack, Titanium alloys in total joint replacement - a materials science perspective, Biomaterials 19 (1998) 1621–1639, https://doi.org/10.1016/S0142-9612(97)00146-4.

[5] L.-Y. Chen, Y.-W. Cui, L.-C. Zhang, Recent development in beta titanium alloys for biomedical applications, Metals 10 (2020) 1139, https://doi.org/10.3390/met10091139.

[6] M. Kaur, K. Singh, Review on titanium and titanium based alloys as bio materials for orthopaedic applications, Mat. Sci. Eng. C 102 (2019) 844–862, https://doi.org/10.1016/j.msec.2019.04.064.

[7] C.S. Pitchi, A. Priyadarshini, G. Sana, S.K.R. Narala, A review on alloy composition and synthesis of β-Titanium alloys for biomedical applications, Mater. Today:. Proc. 26 (2020) 3297–3304, https://doi.org/10.1016/j.matpr.2020.02.468.

[8] S. Tamilselvi, V. Raman, N. Rajendran, Corrosion behaviour of Ti-6Al-7Nb and Ti-6Al-4V ELI alloys in the simulated body fluid solution by electrochemical impedance spectroscopy, Electrochim. Acta 52 (2006) 839–846, https://doi.org/10.1016/j.electacta.2006.06.018.

[9] S.L. Assis, I. Costa, Electrochemical evaluation of Ti-13Nb-13Zr, Ti-6Al-4V and Ti-6Al-7Nb alloys for biomedical application by long-term immersion tests, Mater. Corros. 58 (2007) 329–333, https://doi.org/10.1002/maco.200604027.

[10] S.B. Goodman, J. Gallo, E. Gibon, M. Takagi, Diagnosis and management of implant debris-associated inflammation, Expert Rev. Med. Devices 17 (2020) 41–56, https://doi.org/10.1080/17434440.2020.1702024.

[11] K. Choi, J.L. Kuhn, M.J. Ciarelli, S.A. Goldstein, The elastic moduli of human subchondral, trabecular, and cortical bone tissue and the size-dependency of cortical bone modulus, J. Biomech. 23 (1990) 1103–1113, https://doi.org/10.1016/0021-9290(90)90003-L.

[12] J.-Y. Rho, L. Kuhn-Spearing, P. Zioupos, Mechanical properties and the hierarchical structure of bone, Med. Eng. Phys. 20 (1998) 92–102, https://doi.org/10.1016/S1350-4533(98)00007-1.

[13] M. Niinomi, M. Nakai, Titanium-based biomaterials for preventing stress shielding between implant devices and bone, Int. J. Biomater. (2011) 1–10.

[14] D. Savio, A. Bagno, When the total hip replacement fails: a review on the stress-shielding effect, Processes 10 (2022) 612, https://doi.org/10.3390/pr10030612.

[15] U.S. Department of Health and Human Services, Agency for Toxic Substances and Disease Registry (ATSDR), Toxicological Profile for Vandium (2012). https://wwwn.cdc.gov/TSP/ToxProfiles/ToxProfiles.aspx?id=276&tid=50.

[16] B.C. Costa, C.K. Tokuhara, L.A. Rocha, R.C. Oliveira, P.N. Lisboa-Filho, J.C. Pessoa, Vanadium ionic species from degradation of Ti-6Al-4V metallic implants: In vitro cytotoxicity and speciation evaluation, Mat. Sci. Eng. C 96 (2019) 730–739, https://doi.org/10.1016/j.msec.2018.11.090.

[17] D.R. Crapper, S.S. Krishnan, A.J. Dalton, Brain aluminum distribution in alzheimer's disease and experimental neurofibrillary degeneration, Science 180 (1973) 511–513, https://doi.org/10.1126/science.180.4085.511.

[18] M. Kawahara, K. Muramoto, K. Kobayashi, H. Mori, Y. Kuroda, Aluminum promotes the aggregation of alzheimer's amyloid β-protein in vitro, Biochem. Biophys. Res. Commun. 198 (1994) 531–535, https://doi.org/10.1006/bbrc.1994.1078.

[19] J. Nie, Exposure to Aluminum in Daily Life and Alzheimer's Disease, in: Q. Niu (Ed.), Neurotoxicity of Aluminum, Springer Nature Singapore, Singapore, 2023, pp. 107–121.

[20] M. Niinomi, Recent research and development in titanium alloys for biomedical applications and healthcare goods, Sci. Tech. Adv. Mater. 4 (2003) 445–454, https://doi.org/10.1016/j.stam.2003.09.002.

[21] L.-C. Zhang, L.-Y. Chen, A review on biomedical titanium alloys: recent progress and prospect, Adv. Eng. Mater. 21 (2019) 1801215, https://doi.org/10.1002/adem.201801215.

[22] N. Ma, S. Liu, W. Liu, L. Xie, D. Wei, L. Wang, L. Li, B. Zhao, Y. Wang, Research progress of titanium-based high entropy alloy: methods, properties, and applications, Front. Bioeng. Biotechnol. 8 (2020), 603522, https://doi.org/10.3389/fbioe.2020.603522.

[23] J. Feng, Y. Tang, J. Liu, P. Zhang, C. Liu, L. Wang, Bio-high entropy alloys: progress, challenges, and opportunities, Front. Bioeng. Biotechnol. 10 (2022), 977282, https://doi.org/10.3389/fbioe.2022.977282.

[24] T. Ishimoto, R. Ozasa, K. Nakano, M. Weinmann, C. Schnitter, M. Stenzel, A. Matsugaki, T. Nagase, T. Matsuzaka, M. Todai, H.S. Kim, T. Nakano, Development of TiNbTaZrMo bio-high entropy alloy (BioHEA) super-solid solution by selective laser melting, and its improved mechanical property and biocompatibility, Scr. Mater. 194 (2021), 113658, https://doi.org/10.1016/j.scriptamat.2020.113658.

[25] K. Zhuravleva, Porous ß-type Ti-Nb alloy for biomedical applications, University of Dresden (Germany), 2014. PhD Thesis,.

[26] A. Gebert, D. Eigel, P.F. Gostin, V. Hoffmann, M. Uhlemann, A. Helth, S. Pilz, R. Schmidt, M. Calin, M. Göttlicher, M. Rohnke, J. Janek, Oxidation treatments of beta-type Ti-40Nb for biomedical use, Surf. Coat. Technol. 302 (2016) 88–99.

[27] H.Y. Kim, S. Miyazaki, Martensitic transformation and superelastic properties of Ti-Nb base alloys, Mat. Trans. 56 (2015) 625–634, https://doi.org/10.2320/matertrans.M2014454.

[28] P.A.B. Kuroda, L. Monteiro da Silva, K. dos Santos Jorge, T.A.G. Sousa, C.R.G. Donato, Preparation, structural, microstructural, mechanical, and cytotoxic characterization of Ti-15Nb alloy for biomedical applications, Artif. Organs 44 (2020) 811–817, https://doi.org/10.1111/aor.13624.

[29] C. Schulze, M. Weinmann, C. Schweigel, O. Keßler, R. Bader, Mechanical Properties of a Newly Additive Manufactured Implant Material Based on Ti-42Nb, Materials 11 (2018) 124, doi: 10.3390%2Fma11010124.

[30] Y.L. Zhou, M. Niinomi, T. Akahori, Effects of Ta content on Young's modulus and tensile properties of binary Ti–Ta alloys for biomedical applications, Mat. Sci. Eng. A 371 (2004) 283–290, https://doi.org/10.1016/j.msea.2003.12.011.

[31] H. Prigent, P. Pellen-Mussi, G. Cathelineau, M. Bonnaure-Mallet, Evaluation of the biocompatibility of titanium-tantalum alloy versus titanium, J. Biomed. Mat. Res. 39 (1998) 200–206, https://doi.org/10.1002/(SICI)1097-4636(199802)39:2%3C200::AID-JBM5%3E3.0.CO;2-T.

[32] N. Soro, E.G. Brodie, A. Abdal-hay, A.Q. Alali, D. Kent, M.S. Dargusch, Additive manufacturing of biomimetic Titanium-Tantalum lattices for biomedical implant applications, Mater. Des. 218 (2022), 110688, https://doi.org/10.1016/j.matdes.2022.110688.

[33] S. Huang, S.L. Sing, G. de Looze, R. Wilson, W.Y. Yeong, Laser powder bed fusion of titanium-tantalum alloys: compositions and designs for biomedical applications, J. Mech. Behav. Biomed. Mater. 108 (2020), 103775, https://doi.org/10.1016/j.jmbbm.2020.103775.

[34] E. Eisenbarth, D. Velten, M. Müller, R. Thull, J. Breme, Biocompatibility of beta-stabilising elements of titanium alloys, Biomaterials 25 (2004) 5705–5713, https://doi.org/10.1016/j.biomaterials.2004.01.021.

[35] R.P. Kolli, A. Devaraj, A review of metastable beta titanium alloys, Metals 8 (2018) 506, https://doi.org/10.3390/met8070506.

[36] W. Weng, A. Biesiekierski, Y. Li, C. Wen, Effects of selected metallic and interstitial elements on the microstructure and mechanical properties of beta titanium alloys for orthopedic applications, Materialia 6 (2019), 100323, https://doi.org/10.1016/j.mtla.2019.100323.

[37] T. Ozaki, H. Matsumoto, S. Watanabe, S. Hanada, Beta Ti alloys with low young's modulus, Mater. Trans. 45 (2004) 2776–2779, https://doi.org/10.2320/matertrans.45.2776.

[38] S. Dubinskiy, V. Brailovski, S. Prokoshkin, V. Pushin, K. Inaekyan, V. Sheremetyev, M. Petrzhik, M. Filonov, Structure and properties of Ti-19.7Nb-5.8Ta shape memory alloy subjected to thermomechanical processing including aging, J. Mater. Eng. Perform. 22 (2013) 2656–2664, https://doi.org/10.1007/s11665-013-0555-6.

[39] H.Y. Kim, S. Hashimoto, J.I. Kim, T. Inamura, H. Hosoda, S. Miyazaki, Effect of Ta addition on shape memory behavior of Ti–22Nb alloy, Mat. Sci. Eng. A 417 (2006) 120–128, https://doi.org/10.1016/j.msea.2005.10.065.

[40] V.A. Sheremetyev, S.D. Prokoshkin, V. Brailovski, S.M. Dubinskiy, A.V. Korotitskiy, M.R. Filonov, M.I. Petrzhik, Investigation of the structure stability and superelastic behavior of thermomechanically treated Ti–Nb–Zr and Ti–Nb–Ta shape-memory alloys, Phys. Metals Metallogr. 116 (2015) 413–422, https://doi.org/10.1134/S0031918X15040158.

[41] E. Bertrand, P. Castany, T. Gloriant, Investigation of the martensitic transformation and the damping behavior of a superelastic Ti–Ta–Nb alloy, Acta Mater. 61 (2013) 511–518, https://doi.org/10.1016/j.actamat.2012.09.065.

[42] E. Bertrand, T. Gloriant, D.M. Gordin, E. Vasilescu, P. Drob, C. Vasilescu, S.I. Drob, Synthesis and characterisation of a new superelastic Ti–25Ta–25Nb biomedical alloy, J. Mech. Behav. Biomed. Mater. 3 (2010) 559–564, https://doi.org/10.1016/j.jmbbm.2010.06.007.

[43] A.H. Hussein, M.A.-H. Gepreel, M.K. Gouda, A.M. Hefnawy, S.H. Kandil, Biocompatibility of new Ti–Nb–Ta base alloys, Mat. Sci. Eng. C 61 (2016) 574–578, https://doi.org/10.1016/j.msec.2015.12.071.

[44] J. Liu, L. Chang, H. Liu, Y. Li, H. Yang, J. Ruan, Microstructure, mechanical behavior and biocompatibility of powder metallurgy Nb-Ti-Ta alloys as biomedical material, Mat. Sci. Eng. C 71 (2017) 512–519, https://doi.org/10.1016/j.msec.2016.10.043.

[45] L.V.M. Antony, R.G. Reddy, Processes for production of high-purity metal powders, JOM 55 (2003) 14–18, https://doi.org/10.1007/s11837-003-0153-4.

[46] M. Hohmann, L. Norbert, System for the production of powders from metals, US Patent US5284329 (A) (1994).

[47] L.E. Murr, Metallurgy principles applied to powder bed fusion 3D printing/additive manufacturing of personalized and optimized metal and alloy biomedical implants: an overview, J. Mater. Res. Technol. 9 (2020) 1087–1103, https://doi.org/10.1016/j.jmrt.2019.12.015.

[48] Y. Chen, W. Li, C. Zhang, Z. Wu, J. Liu, Recent developments of biomaterials for additive manufacturing of bone scaffolds, Adv. Healthc. Mater. 9 (2020) 2000724, https://doi.org/10.1002/adhm.202000724.

[49] M. Javaid, A. Haleem, Additive manufacturing applications in orthopaedics: A review, J. Clin. Orthop. Trauma. 9 (2018) 202–206, https://doi.org/10.1016/j.jcot.2018.04.008.

[50] K.C. Wong, 3D-printed patient-specific applications in orthopedics, Orthop. Res. Rev. 8 (2016) 57–66, https://doi.org/10.2147/ORR.S99614.

[51] M. Weinmann, H. Brumm, C. Schnitter, M. Stenzel, Metal Powder for 3D Printing, US Patent US2022023941 (A1) (2022).

[52] T.C. Dzogbewu, W. Bouwer du Preez, Additive manufacturing of Ti-based intermetallic alloys: a review and conceptualization of a next-generation machine, Materials 14 (2021) 4317, https://doi.org/10.3390/ma14154317.

[53] D.K. Do, P. Li, The effect of laser energy input on the microstructure, physical and mechanical properties of Ti-6Al-4V alloys by selective laser melting, Virtual Phys. Prototyp. 11 (2016) 41–47, https://doi.org/10.1080/17452759.2016.1142215.

[54] https://www.icdd.com/pdf-2/.

[55] https://www.zwickroell.com/de/produkte/statische-material-pruefmaschinen/universalpruefmaschinen-fuer-statische-anwendungen/allroundline/.

[56] ASTM B213-20, Standard Test Methods for Flow Rate of Metal Powders Using the Hall Flowmeter Funnel, https://www.astm.org/b0213-20.html.

[57] J. Markhoff, M. Weinmann, C. Schulze, R. Bader, Influence of different grained powders and pellets made of Niobium and Ti-42Nb on human cell viability, Mat. Sci. Eng. C 73 (2017) 756–766, https://doi.org/10.1016/j.msec.2016.12.098.

[58] C. Lauhoff, T. Arold, A. Bolender, M.W. Rackel, F. Pyczak, M. Weinmann, W. Xu, A. Molotnikov, T. Niendorf, Microstructure of an additively manufactured Ti-Ta-Al alloy using novel pre-alloyed powder feedstock material, Addit. Manuf. Lett. 6 (2023), 100144, https://doi.org/10.1016/j.addlet.2023.100144.

[59] G. Bartzsch, S. Scherbring, J. Richter, M. Vollmer, J. Mola, T. Niendorf, O. Volkova, Gas atomization of Al-steels, Mater. Today Commun. 34 (2023), 105388, https://doi.org/10.1016/j.mtcomm.2023.105388.

[60] P.A. Hooper, Melt pool temperature and cooling rates in laser powder bed fusion, Addit. Manuf. 22 (2018) 548–559, https://doi.org/10.1016/j.addma.2018.05.032.

[61] C. Leyens, M. Peters (EDS.), Titanium and Titanium Alloys - Fundamental and Applications, Wiley-VCH (2003), doi: 10.1002/3527602119.

[62] D. Bhattacharyya, G.B. Viswanathan, R. Denkenberger, D. Furrer, H.L. Fraser, The role of crystallographic and geometrical relationships between α and β phases in an α/β titanium alloy, Acta Mater. 51 (2003) 4679–4691, https://doi.org/10.1016/S1359-6454(03)00179-4.

[63] T. Ahmed, H.J. Rack, Phase transformations during cooling in α+β titanium alloys, Mater. Sci. Eng. A 243 (1998) 206–211, https://doi.org/10.1016/S0921-5093(97)00802-2.

[64] J.W. Elmer, T.A. Palmer, S.S. Babu, W. Zhang, Phase transformation dynamics during welding of Ti–6Al–4V, J. Appl. Phys. 95 (2004) 8327-8339, doi: 10.1063/1.1737476.

[65] H.Y. Kim, Y. Ikehara, J.I. Kim, H. Hosoda, S. Miyazaki, Martensitic transformation, shape memory effect and superelasticity of Ti–Nb binary alloys, Acta Mater. 54 (2006) 2419–2429, https://doi.org/10.1016/j.actamat.2006.01.019.

[66] K.A. Bywater, J.W. Christian, Martensitic transformations in titanium-tantalum alloys, Phil. Mag. 8 (1972) 1249–1273, https://doi.org/10.1080/14786437208223852.

[67] H.W. Jeong, Y.S. Yoo, Y.T. Lee, J.K. Park, Elastic softening behavior of Ti–Nb single crystal near martensitic transformation temperature, J. Appl. Phys. 108 (2010) 063515, doi: 10.1063/1.3486212.

[68] S. Banumathy, R.K. Mandal, A.K. Singh, Structure of orthorhombic martensitic phase in binary Ti–Nb alloys, J. Appl. Phys. 106 (2009) 093518, doi: 10.1063/1.3255966.

[69] B. Dutta, F.H. Froes, The additive manufacturing (AM) of titanium alloys, Met. Powder Rep. 72 (2017) 96–106, https://doi.org/10.1016/j.mprp.2016.12.062.

[70] M.E. Glicksman, Principles of solidification: an introduction to modern casting and crystal growth concepts, Springer New York, NY, ISBN 978-1-4899-8185-1 (2014), doi: 10.1007/978-1-4419-7344-3.

[71] L. Thijs, M.L. Montero Sistiaga, R. Wauthle, Q. Xie, J.-P. Kruth, J.V. Humbeeck, Strong morphological and crystallographic texture and resulting yield strength anisotropy in selective laser melted tantalum, Acta Mater. 61 (2013) 4657–4668, https://doi.org/10.1016/j.actamat.2013.04.036.

[72] Z. Zheng, X. Jin, Y. Bai, Y. Yang, C. Ni, W.F. Lu, H. Wang, Microstructure and anisotropic mechanical properties of selective laser melted Ti6Al4V alloy under different scanning strategies, Mat. Sci. Eng. A 831 (2022) 142236.

[73] C. Lauhoff, N. Sommer, M. Vollmer, G. Mienert, P. Krooß, S. Böhm, T. Niendorf, Excellent superelasticity in a Co-Ni-Ga high-temperature shape memory alloy processed by directed energy deposition, Mat. Res. Lett. 8 (2020) 314–320, https://doi.org/10.1080/21663831.2020.1756495.

[74] T. Niendorf, S. Leuders, A. Riemer, H.A. Richard, T. Tröster, D. Schwarze, Highly anisotropic steel processed by selective laser melting, Met. Mat. Trans. B 44 (2013) 794–796, https://doi.org/10.1007/s11663-013-9875-z.

[75] F. Brenne, A. Taube, M. Pröbstle, S. Neumeier, D. Schwarze, M. Schaper, T. Niendorf, Microstructural design of Ni-base alloys for high temperature applications – impact of heat treatment on microstructure and mechanical properties after Selective Laser Melting, Prog. Addit. Manuf. 1 (2016) 141–151, https://doi.org/10.1007/s40964-016-0013-8.

[76] E.G. Brodie, T. Wegener, J. Richter, A. Medvedev, T. Niendorf, A. Molotnikov, A mechanical comparison of alpha and beta phase biomedical TiTa lattice structures, Mater. Des. 212 (2021), 110220, https://doi.org/10.1016/j.matdes.2021.110220.